Journal of Engineering Mathematics (2024) 147:12
https://doi.org/10.1007/s10665-024-10383-x

Lubrication flow in grinding

Zak Crowson[1] · John Billingham[1] · Paul Houston[1]

Received: 1 March 2024 / Accepted: 3 July 2024

Abstract
In the machining process known as grinding, fluid is applied to regulate the temperature of the workpiece and reduce the risk of expensive thermal damage. The factors that influence the transport of this grinding fluid are not well understood; however, it is important to gain understanding in order to try to avoid the unnecessary cost incurred from its inefficient application. In this work, we use the method of matched asymptotic expansions to derive the multiscale system of equations that governs the flow. Under the lubrication approximation, we show that it is possible to calculate the flow rate through the grinding zone without having to solve for the flow far from the grinding zone. Additional empirically determined boundary conditions do not need to be imposed. With this lubrication model, we quantify the effect of experimental parameters on the flow field in the grinding zone and study how the flow regime responds to changes in these parameters.

Keywords Grinding · Lubrication · Matched asymptotic expansions · Reynolds equation

1 Introduction

Grinding is a machining process in which a material, referred to as the workpiece, is fed into the path of a grinding wheel composed of hard abrasives. Grinding is used for several different purposes, but primarily for cutting, where large amounts of the workpiece are removed, and finishing, where the rough surface of the workpiece is smoothed. The thickness of the surface layer removed during grinding is known as

John Billingham and Paul Houston have contributed equally to this work.

✉ Zak Crowson
zak.crowson2@nottingham.ac.uk

John Billingham
john.billingham@nottingham.ac.uk

Paul Houston
paul.houston@nottingham.ac.uk

[1] School of Mathematical Sciences, University of Nottingham, University Park, Nottingham, Nottinghamshire NG7 2RD, UK

Published online: 25 July 2024

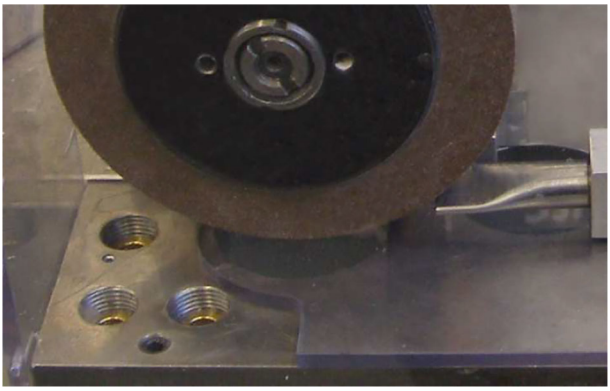

Fig. 1 A simulated grinding setup with a narrow gap between the clockwise-rotating grinding wheel and flat perspex workpiece. Grinding fluid is ejected from the nozzle on the right-hand side towards the gap underneath the grinding wheel

the depth of cut. During grinding, the region of contact between grinding wheel and workpiece, referred to as the grinding zone, can experience temperatures of up to 1000 °C [1]. To reduce the risk of thermal damage to the workpiece, a grinding fluid is commonly applied to the grinding zone to lubricate and cool the workpiece. However, the mechanics of this flow are poorly understood, resulting in inefficient grinding fluid application which is estimated to account for up to 17% of the cost of each grinding operation [2]. Understanding the impact that grinding parameters have on the features of the flow is key to reducing grinding fluid waste.

The space between abrasives plays an important role in transporting fluid to the grinding zone [3]. Engineer et al. [4] experimentally investigated the effect of various grinding parameters on the flow rate of grinding fluid through the grinding zone. They observed that an increase in the grinding wheel's porosity led to an increase in the flow rate.

Existing mathematical descriptions of the transport of grinding fluid assume that the spaces between the abrasives form an effective gap between the workpiece and the grinding wheel. More precisely, they consider simulated grinding where the grinding wheel is taken to spin at a non-zero distance above the flat workpiece such that no contact is made between the two surfaces, i.e. zero depth of cut. An image of a simulated grinding setup is shown in Fig. 1.

A common approach is to model the flow in this effective gap with the Reynolds equation. Originally derived by Reynolds [5], the one-dimensional Reynolds equation is

$$\frac{\partial}{\partial x}\left(\frac{h^3}{\mu}\frac{\partial p}{\partial x}\right) = 6\,(u_1 + u_2)\,\frac{\partial h}{\partial x} + 12\frac{\partial h}{\partial t}, \tag{1}$$

whose dependent variable is the pressure distribution, $p(x, t)$, in the gap between two surfaces separated by an a-priori known distance, $h(x, t)$. Here, u_1 and u_2 are the speeds of the two surfaces and μ the dynamic viscosity of the fluid. The key assump-

tions in the derivation of (1) are that the fluid is incompressible and Newtonian, the gap between the surfaces is narrow enough that viscous forces dominate over inertial forces and that the effect of gravity is negligible. This is known as the lubrication approximation. An in-depth study of the lubrication approximation with applications can be found in [6, pp. 294–346]. Extensions to the lubrication approximation exist which widen its applicability in flows where one or more of the standard assumptions are not valid. For example, allowing for steep boundary gradients by including higher-order corrections terms [7] or inertial effects by applying boundary-layer theory along the gap [8].

One shortcoming of current approaches is the need for empirically determined measurements to close the model. Schumack et al. [9] considered the two dimensional stream function form of the steady Navier–Stokes equations at small Reynolds numbers. Instead of allowing the grinding wheel to spin at high speeds, it was held stationary and an infinitely long, planar workpiece translated at a typical grinding wheel speed. They treated the grinding fluid as incompressible and remarked that "pressure is small in grinding situations and hence does not influence the viscosity". By assuming that the gap between the grinding wheel and the workpiece was narrow enough that viscous forces dominate over inertial forces, they were able to derive an expression for the pressure in the gap. In order to close their problem, empirically determined flow rates had to be prescribed at artificial boundaries.

Hryniewicz et al. [10, 11] built upon the work of Schumack et al. by considering the effect that surface roughness of the grinding wheel has on the pressure in the grinding zone. To incorporate the effects of roughness, they used a volume averaging technique on the leading order Reynolds equation at moderate Reynolds number, and equated the distance between the bottom of the grinding wheel and the workpiece in their model with the minimum distance between the grinding wheel abrasives and the workpiece in their experiments. As the focus was only the hydrodynamic pressure in the grinding zone, they encountered the same difficulties as Schumack et al. when attempting to solve for the velocity field— the need for empirically determined boundary conditions. Furthermore, their results exhibit a similar breakdown of accuracy when inertial effects become relevant at higher Reynolds numbers. There are many studies that use the idea of modelling the flow in the grinding zone using the Reynolds equation, applying empirically determined boundary conditions at artificial boundaries. In these works, the workpiece is consistently assumed to be a planar surface; see, for example, [12] and [13].

Simpler mathematical models exist for the transport of grinding fluid; however, these models have a narrow output. Gviniashvili et al. [14] developed a model for predicting the flow rate through the grinding zone. The model is based on the balance of momentum by assuming that the grinding fluid exiting the nozzle adheres to the grinding wheel's velocity on impact. Empirical coefficients, which are thought to depend on the structure of the grinding wheel and rheology of the grinding fluid, then account for the difference observed between the theoretical and experimental flow rates.

In the grinding zone, many physical and chemical processes can influence the transport of grinding fluid. Two such examples are film boiling [15] and surface layer formation [16, pp. 502–505], the effects of which are not well understood. We will try

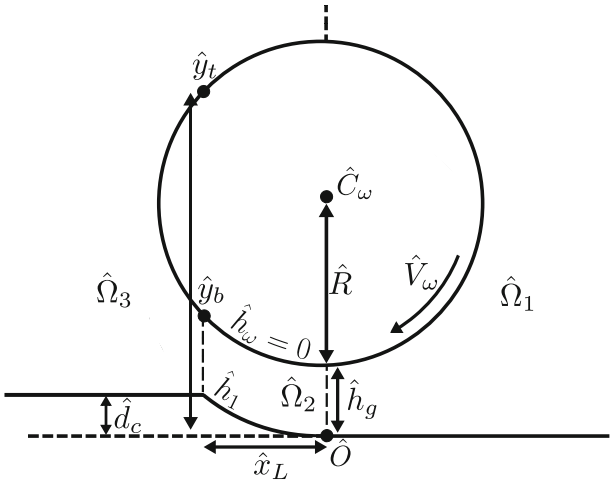

Fig. 2 Illustration of introduced quantities in our problem setup

to account for these effects to some extent by assuming (Navier) slip on both grinding wheel and workpiece surfaces, [17]. Previous work by Wichmann et al. on the thin-film wetting of grinding wheels has observed a dependency of the slip length on the grinding wheel's abrasive size [18].

In this paper, we consider the problem of simulated grinding with a smooth, spinning wheel situated a small distance above a workpiece. This gap characterises the mean void space between the grinding wheel and the workpiece. The grinding zone is taken to be a curved channel with the same shape as the grinding wheel. Due to the way the cutting is performed in grinding, this is a simplification of physical grinding zone geometries. See, e.g. [19] which presents detailed scans of workpiece and grinding wheel surfaces after undergoing grinding, showing irregular surface profiles. However, the grinding zone geometry we consider here represents a preliminary and necessary step towards developing more comprehensive models for predicting the transport of grinding fluid during grinding.

We assume an incompressible grinding fluid fills the domain. To model the flow under the grinding wheel, we use the ratio of the separation of the gap between the grinding wheel and the workpiece, $\hat{h}_g$, and the radius of the wheel, $\hat{R}$, as the small parameter in the method of matched asymptotic expansions (see Fig. 2). We split the flow into two separate domains over these length scales and derive a system of lubrication equations governing the flow under the grinding wheel. We find that this flow is independent of the flow over the longer length scale, which gives our approach two primary advantages over existing models. The first is the ability to solve for the flow in the grinding zone without requiring empirically determined boundary conditions to formulate a closed problem. The second is that the shape of the grinding zone is more accurately treated as a channel with non-zero curvature, representing the workpiece under grinding, rather than a planar workpiece.

2 Problem formulation

We use hat notation to denote dimensional quantities and model a circular grinding wheel of radius $\hat{R}$ located above the workpiece with standoff distance $\hat{h}_g > 0$, as shown in Fig. 2. The origin, $\hat{O}$, of a Cartesian coordinate system, $(\hat{x}, \hat{y})$, is the point on the workpiece directly below the centre of the grinding wheel, $\hat{C}_\omega$. The grinding wheel rotates clockwise, with speed $\hat{V}_\omega$ at its surface, and we assume that the velocity of the workpiece is negligible relative to that of the grinding wheel. The workpiece has a smooth curved surface along the region of contact, i.e. the grinding zone, and planar surfaces at $\hat{y} = \hat{d}_c$ and $\hat{y} = 0$ to the left and right of the grinding zone, respectively. The depth of cut is $\hat{d}_c \geq 0$. We denote the surface of the workpiece by $\hat{h}_1(\hat{x})$. The surface of the grinding wheel is given implicitly by $\hat{h}_\omega(\hat{x}, \hat{y}) = 0$, where $\hat{h}_\omega(\hat{x}, \hat{y}) = \hat{x}^2 + \left(\hat{y} - 1 - \hat{h}_g\right)^2 - 1$. The height of the bottom half of the grinding wheel is denoted by $\hat{h}_2(\hat{x})$. The flow domain, which surrounds the grinding wheel and workpiece, is $\hat{\Omega} = \hat{\Omega}_1 \cup \hat{\Omega}_2 \cup \hat{\Omega}_3$. We consider the flow of an incompressible Newtonian fluid in $\hat{\Omega}$. The fluid has constant density $\hat{\rho}$ and viscosity $\hat{\mu}$, with fluid velocity $\hat{\boldsymbol{u}} = \hat{u}_x \boldsymbol{e}_x + \hat{u}_y \boldsymbol{e}_y$ and pressure $\hat{p}$. On $\hat{h}_1$ and $\hat{h}_\omega$, we assume that there is slip of the grinding fluid with slip length $\hat{\beta}$.

Some dimensionless parameters that we will use below are

$$\varepsilon = \frac{\hat{h}_g}{\hat{R}}, \qquad \gamma = \frac{\hat{d}_c}{\hat{R}}, \qquad \delta = \frac{\gamma}{\varepsilon} = \frac{\hat{d}_c}{\hat{h}_g}, \qquad \mathrm{Re} = \frac{\hat{\rho}\hat{V}_\omega\hat{R}}{\hat{\mu}}, \qquad \beta = \frac{\hat{\beta}}{\hat{R}}. \tag{2}$$

If $\gamma = \delta = 0$, the workpiece is a planar surface. In a typical surface grinding regime [20],

$$\varepsilon = 5 \times 10^{-5}, \qquad \delta = 2, \qquad \mathrm{Re} = 1 \times 10^5, \tag{3}$$

and in a typical creep-feed grinding regime [21],

$$\varepsilon = 2.5 \times 10^{-3}, \qquad \delta = 4.8, \qquad \mathrm{Re} = 1 \times 10^5. \tag{4}$$

For surfaces with low degrees of roughness, experiments have found that typically

$$0 < \hat{\beta} < 1 \times 10^{-5}\,\mathrm{m}, \tag{5}$$

see [17] for an overview of experimentally measured slip lengths. In practice, with the rough surfaces used in grinding, slip is likely to be present over the lengthscale characterising the abrasive size, for which $\hat{h}_g$ provides a first approximation of. Hence, we suppose $\hat{\beta}$ will be near or larger than the upper bound of (5) and consider the asymptotic solution in the limit

$$\delta = O(1), \qquad \mathrm{Re} = O\left(\varepsilon^{-1}\right), \qquad \beta = O(\varepsilon) \quad \text{as } \varepsilon \to 0, \tag{6}$$

which is broadly consistent with the parameter estimates (3) and (4).

2.1 Dimensionless problem

We introduce the dimensionless variables

$$x = \frac{\hat{x}}{\hat{R}}, \qquad y = \frac{\hat{y}}{\hat{R}}, \qquad t = \frac{\hat{V}_\omega}{\hat{R}}\hat{t}, \qquad \boldsymbol{u} = \frac{\hat{\boldsymbol{u}}}{\hat{V}_\omega}, \qquad p = \frac{\varepsilon^{3/2}\hat{R}}{\hat{\mu}\hat{V}_\omega}\hat{p}. \tag{7}$$

The dimensionless flow domain is $\Omega = \Omega_1 \cup \Omega_1 \cup \Omega_3$, where

$$\begin{aligned} \Omega_1 = &\{(x,y) : x \geq 0,\ y \in (0, y_b) \cup (y_t, \infty),\ h_\omega(x,y) > 0\} \\ &\cup \{(x,y) : x \geq 0,\ y \in [y_b, y_t],\ h_\omega(x,y) > 0\}, \end{aligned} \tag{8}$$

$$\Omega_2 = \left\{(x,y) : x \in (x_L, 0),\ y \in \left(h_1(x), h_2(x)\right)\right\}, \tag{9}$$

$$\begin{aligned} \Omega_3 = &\{(x,y) : x \leq x_L,\ y \in (\gamma, y_b) \cup (y_t, \infty),\ h_\omega(x,y) > 0\} \\ &\cup \{(x,y) : x \leq x_L,\ y \in [y_b, y_t],\ h_\omega(x,y) > 0\} \\ &\cup \{(x,y) : x \in (x_L, 0),\ y > y_t,\ h_\omega(x,y) > 0\}, \end{aligned} \tag{10}$$

represents the flow domain to the right of the grinding zone, the grinding zone and left of the grinding zone, respectively, with

$$y_b = 1 + \varepsilon - \sqrt{1 - x_L^2}, \qquad y_t = 1 + \varepsilon + \sqrt{1 - x_L^2}. \tag{11}$$

The dimensionless form of the location of the boundaries is

$$h_1(x) = \begin{cases} 0 & \text{for } x \geq 0, \\ 1 + \varepsilon - \sqrt{(1+\varepsilon)^2 - x^2} & \text{for } x \in (x_L, 0), \\ \gamma & \text{for } x \leq x_L, \end{cases} \tag{12}$$

$$h_2(x) = 1 + \varepsilon - \sqrt{1 - x^2}, \tag{13}$$

$$h_\omega(x,y) = x^2 + (y - 1 - \varepsilon)^2 - 1, \tag{14}$$

$$x_L = -(1+\varepsilon)\sqrt{1 - \left(1 - \frac{\gamma}{1+\varepsilon}\right)^2}. \tag{15}$$

The dimensionless Navier–Stokes equations are

$$\nabla \cdot \boldsymbol{u} = 0, \tag{16}$$

$$\varepsilon^{3/2}\mathrm{Re}\left(\frac{\partial \boldsymbol{u}}{\partial t} + \boldsymbol{u} \cdot \nabla \boldsymbol{u}\right) = -\nabla p + 2\varepsilon^{3/2}\nabla \cdot \boldsymbol{E}, \tag{17}$$

to be solved subject to the slip conditions

$$\boldsymbol{u} - \boldsymbol{t} = 2\beta \boldsymbol{n} \cdot \boldsymbol{E} \cdot (\boldsymbol{I} - \boldsymbol{nn}) \qquad \text{on } h_\omega(x,y) = 0, \tag{18}$$

$$\boldsymbol{u} = 2\beta \boldsymbol{n} \cdot \boldsymbol{E} \cdot (\boldsymbol{I} - \boldsymbol{nn}) \qquad \text{on } y = h_1(x), \tag{19}$$

and far-field conditions

$$\boldsymbol{u} \to \boldsymbol{0} \qquad \text{as } x \to \pm\infty,\ y \to \infty, \tag{20}$$

$$p \to 0 \qquad \text{as } x \to \pm\infty,\ y \to \infty. \tag{21}$$

Here, $\boldsymbol{E} = \frac{1}{2}\left(\nabla \boldsymbol{u} + (\nabla \boldsymbol{u})^T\right)$ is the rate of strain tensor, $\boldsymbol{I}$ is the metric tensor, $\boldsymbol{t} = t_x \boldsymbol{e}_x + t_y \boldsymbol{e}_y$ is the unit tangent to $h_\omega(x, y) = 0$ with

$$t_x = \begin{cases} \sqrt{1 - x^2} & \text{for } y > 1 + \varepsilon, \\ -\sqrt{1 - x^2} & \text{for } y \le 1 + \varepsilon, \end{cases} \tag{22}$$

$$t_y = -x \tag{23}$$

and $\boldsymbol{n} = n_x \boldsymbol{e}_x + n_y \boldsymbol{e}_y$ is the inward unit normal to the surface, given by

$$n_x = -x, \tag{24}$$

$$n_y = \begin{cases} -\sqrt{1 - x^2} & \text{for } y > 1 + \varepsilon, \\ \sqrt{1 - x^2} & \text{for } y \le 1 + \varepsilon, \end{cases} \tag{25}$$

on $h_\omega(x, y) = 0$ and

$$n_x = 0 \quad \text{for } x \ge 0, \tag{26}$$

$$n_y = 1 \quad \text{for } x \ge 0, \tag{27}$$

$$n_x = -\frac{x}{1 + \varepsilon} \quad \text{for } x \in (x_L, 0), \tag{28}$$

$$n_y = \frac{\sqrt{(1 + \varepsilon)^2 - x^2}}{1 + \varepsilon} \quad \text{for } x \in (x_L, 0), \tag{29}$$

$$n_x = 0 \quad \text{for } x \le x_L, \tag{30}$$

$$n_y = 1 \quad \text{for } x \le x_L, \tag{31}$$

on $y = h_1(x)$.

Setting $\varepsilon = 0$ yields a contact problem with incompatible boundary conditions (18) and (19), which cannot both be satisfied. We therefore introduce variables that stretch the small-scale grinding region. A variable rescaling argument leads us to introduce the $O(1)$ stretched variables, denoted by superscript $\star$, as

$$x^\star = \frac{x}{\sqrt{\varepsilon}}, \quad y^\star = \frac{y}{\varepsilon}, \quad u^\star = u, \quad v^\star = \frac{v}{\sqrt{\varepsilon}}, \quad p^\star = p, \quad \beta^\star = \frac{\beta}{\varepsilon}. \tag{32}$$

The grinding zone region, where these stretched variables are of $O(1)$, is an inner region. The rest of the domain of solution, where the variables given by (7) are of $O(1)$, is an outer region.

2.2 Outer problem

The outer problem describes the flow in the outer region where we take $\varepsilon = 0$. In order to balance leading order advection and pressure gradients terms in (17), we must introduce

$$p^o = \frac{p}{\varepsilon^{3/2}\mathrm{Re}}, \tag{33}$$

where $p^o = O(1)$. This means that the outer flow satisfies the full Navier–Stokes equations with large Reynolds number. We will not consider the details of this flow since we find that the leading order flow in the inner region is independent of the flow in the outer region. This is due to the large-scale disparity between the inner and outer pressure, highlighted by (7) and (33), respectively. This results in the outer region pressure appearing as a low order perturbation to the inner region pressure. Therefore, at leading order, the matching condition of the inner and outer region pressure reduces to a homogeneous far-field inner region pressure condition.

2.3 Inner problem

The inner region, $\Omega^\star = \Omega_1^* \cup \Omega_2^* \cup \Omega_3^*$, consists of the three disjoint regions

$$\Omega_1^\star = \left\{ \left(x^\star, y^\star\right) : x^\star > 0,\ y \in \left(0, \frac{1}{2}\left(x^{\star 2} + 2\right)\right) \right\}, \tag{34}$$

$$\Omega_2^\star = \left\{ \left(x^\star, y^\star\right) : x^\star \in \left(x_L^\star, 0\right),\ y \in \left(\frac{x^{\star 2}}{2}, \frac{1}{2}\left(x^{\star 2} + 2\right)\right) \right\}, \tag{35}$$

$$\Omega_3^\star = \left\{ \left(x^\star, y^\star\right) : x^\star < x_L^\star,\ y \in \left(\delta, \frac{1}{2}\left(x^{\star 2} + 2\right)\right) \right\}, \tag{36}$$

with boundaries given by

$$h_1^\star\left(x^\star\right) = \begin{cases} 0 & \text{for } x^\star \geq 0, \\ \frac{1}{2}x^{\star 2} & \text{for } x^\star \in \left(x_L^\star, 0\right), \\ \delta & \text{for } x^\star \leq x_L^\star, \end{cases} \tag{37}$$

$$h_2^\star\left(x^\star\right) = \frac{1}{2}\left(x^{\star 2} + 2\right), \tag{38}$$

$$x_L^\star = -\sqrt{2\delta}. \tag{39}$$

We will denote the variables $u^\star$, $v^\star$ and $p^\star$ with subscript i to indicate that they belong to $\Omega_i^\star$ for $i = 1, 2, 3$. In addition, we denote the cross-sectional flow rate in $\Omega_i^\star$ between $y^\star = h_1^\star(x^\star)$ and $y^\star = h_2^\star(x^\star)$ by $Q_i^\star(x^\star, t)$ for $i = 1, 2, 3$.

At leading order, in $\Omega_i^\star$, we have the usual lubrication equations

$$\frac{\partial u_i^\star}{\partial x^\star} + \frac{\partial v_i^\star}{\partial y^\star} = 0, \tag{40}$$

$$\frac{\partial p_i^\star}{\partial x^\star} = \frac{\partial^2 u_i^\star}{\partial y^{\star 2}}, \tag{41}$$

$$\frac{\partial p_i^\star}{\partial y^\star} = 0, \tag{42}$$

subject to the boundary conditions

$$u_i^\star + 1 = -\beta^\star \frac{\partial u_i^\star}{\partial y^\star} \quad \text{on } y^\star = h_2^\star\left(x^\star\right), \tag{43}$$

$$v_i^\star + x^\star = -\beta^\star x^\star \frac{\partial u_i^\star}{\partial y^\star} \quad \text{on } y^\star = h_2^\star\left(x^\star\right), \tag{44}$$

for $i = 1, 2, 3$, and

$$u_1^\star = \beta^\star \frac{\partial u_1^\star}{\partial y^\star} \quad \text{on } y^\star = h_1^\star\left(x^\star\right),\ x^\star \geq 0, \tag{45}$$

$$v_1^\star = 0 \quad \text{on } y^\star = h_1^\star\left(x^\star\right),\ x^\star \geq 0, \tag{46}$$

$$u_2^\star = \beta^\star \frac{\partial u_2^\star}{\partial y^\star} \quad \text{on } y^\star = h_1^\star\left(x^\star\right),\ x^\star \in \left(x_L^\star, 0\right), \tag{47}$$

$$v_2^\star = \beta^\star x^\star \frac{\partial u_2^\star}{\partial y^\star} \quad \text{on } y^\star = h_1^\star\left(x^\star\right),\ x^\star \in \left(x_L^\star, 0\right), \tag{48}$$

$$u_3^\star = \beta^\star \frac{\partial u_3^\star}{\partial y^\star} \quad \text{on } y^\star = h_1^\star\left(x^\star\right),\ x^\star \leq x_L^\star, \tag{49}$$

$$v_3^\star = 0 \quad \text{on } y^\star = h_1^\star\left(x^\star\right),\ x^\star \leq x_L^\star. \tag{50}$$

We have introduced artificial boundaries in the flow domain, so we require additional conditions to enforce continuity of flow rate and pressure

$$Q_1^\star = Q_2^\star, \quad p_1^\star = p_2^\star \quad \text{at } x^\star = 0, \tag{51}$$

$$Q_2^\star = Q_3^\star, \quad p_2^\star = p_3^\star \quad \text{at } x^\star = x_L^\star. \tag{52}$$

To close the inner problem, we need a matching condition for the pressure, and (33) shows that

$$\lim_{x^\star \to \infty} p_1^\star = 0, \qquad \lim_{x^\star \to -\infty} p_3^\star = 0. \tag{53}$$

In other words, the pressure distribution created by the flow in the grinding zone is an order of magnitude larger than that in the outer flow, which therefore has no effect at leading order. In principle, once the flow in the inner region is known, the flow in the outer region can be determined, subject to appropriate flow rate conditions at the inlet and outlet to the grinding zone, which are point sources or sinks on the outer lengthscale.

We will see in the next section that (40)–(53) is a closed problem for the flow in the inner region. As there are no time derivatives at leading order and the matching conditions are independent of time, the flow in the inner region is steady, so we will henceforth assume no dependence on t.

2.4 Leading order analytical solution

From (40)–(53), we have in $\Omega_i^\star$, for $i = 1, 2, 3$,

$$-\frac{x^{\star 2}+2}{4}-\frac{\left[x^{\star 2}+2\left(1+6\beta^\star\right)\right]\left(x^{\star 2}+2\right)^2}{96}\frac{\mathrm{d}p_1^\star}{\mathrm{d}x^\star}=Q^\star, \tag{54}$$

$$-\frac{1}{2}-\frac{1+6\beta^\star}{12}\frac{\mathrm{d}p_2^\star}{\mathrm{d}x^\star}=Q^\star, \tag{55}$$

$$-\frac{x^{\star 2}+2\left(1-\delta\right)}{4}-\frac{\left[x^{\star 2}+2\left(1+6\beta^\star-\delta\right)\right]\left[x^{\star 2}+2\left(1-\delta\right)\right]^2}{96}\frac{\mathrm{d}p_3^\star}{\mathrm{d}x^\star}=Q^\star, \tag{56}$$

where $Q^\star$ denotes the constant cross-sectional flow rate. In addition, we denote the flow rate contribution due to shear effects and pressure gradient in $\Omega_i^\star$ by $Q_{s,i}^\star$ and $Q_{p,i}^\star$, respectively, with

$$Q^\star = Q_{s,i}^\star + Q_{p,i}^\star \tag{57}$$

for $i = 1, 2, 3$. Further information can be found in Appendix A.

Each of Eqs. (54) to (56) is separable, and can be integrated analytically. However, the functional form of (56) leads to five different functional forms for the analytical solution, $p_3^\star$. These can be classified as: I: $0 < \delta < 1$; II: $\delta = 1$; III: $1 < \delta < 1 + 6\beta^\star$; IV: $\delta = 1 + 6\beta^\star$; V: $\delta > 1 + 6\beta^\star$. The pressure solution for each case can be found in Appendix B. In Appendix C , we perform a validation on the lubrication model derived here via comparison of the pressure solution in the inner region to the full-scale problem given by (16)–(21).

We will study the solution of each case in order to understand how the parameters affect the flow rate through the grinding zone.

3 Discussion

The expressions for the pressure given by (B.12), (B.14), (B.15), (B.19), (B.21), (B.23) and (B.25) are a mixture of rational polynomials with inverse trigonometric and inverse hyperbolic functions. The pressure in the grinding zone, $p_2^\star$, is linear. In Fig. 3, we plot the pressure in the inner region, $p^\star$, for various values of δ and $\beta^\star$. For each value of δ shown, the solution converges to the no-slip solution, represented by the red dotted line, in the limit $\beta^\star \to 0$. In contrast, the absolute value of the pressure decreases at every point in the inner region and eventually in the limit $\beta^\star \to \infty$, $p^\star \to 0$.

We remark that a trough of negative (relative) pressure can be observed along the grinding zone. This has been seen to occur in experimental data of simulated grinding,

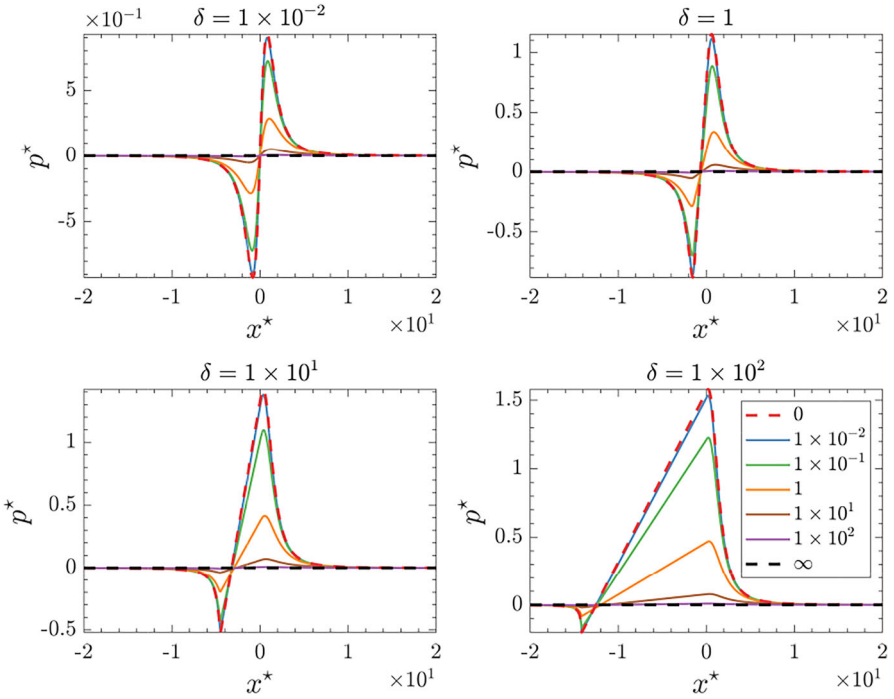

Fig. 3 Plot of the pressure distribution, $p^\star$, in the inner region for different values of δ, shown in the titles. The legend corresponds to the value of $\beta^\star$, the dimensionless slip length

e.g. [10]. However, due to empirical boundary conditions applied to the Reynolds equation in the same work, the flow model failed to capture this feature.

In Fig. 4, we plot $\mathrm{d}p^\star/\mathrm{d}x^\star$ for various values of δ and $\beta^\star$. We observe the same behaviour for all values of δ, namely that as $\beta^\star$ increases, the magnitude of the pressure derivative decreases everywhere. Similarly, we can show that in each regime

$$\lim_{\beta^\star \to \infty} \frac{\mathrm{d}p^\star}{\mathrm{d}x^\star} = 0. \tag{58}$$

We recall that there is no imposed pressure gradient across the inner region from the outer region via (53). Hence, (58) states that in the limit $\beta^\star \to \infty$, the pressure gradient of the flow in the inner region disappears and the flow reduces to a boundary-driven shear flow with constant velocity profile. Similar behaviour is seen in plane Couette flow with full slip on both surfaces where the velocity solution is a constant profile [22].

In Fig. 5, we plot the flow rate, $Q^\star$, as a function of δ for various values of $\beta^\star$.

We can see that as $\beta^\star$ increases, so does $Q^\star$, despite Fig. 4 showing a decrease in the pressure derivative. We can show that the maximum flow rate across all regimes

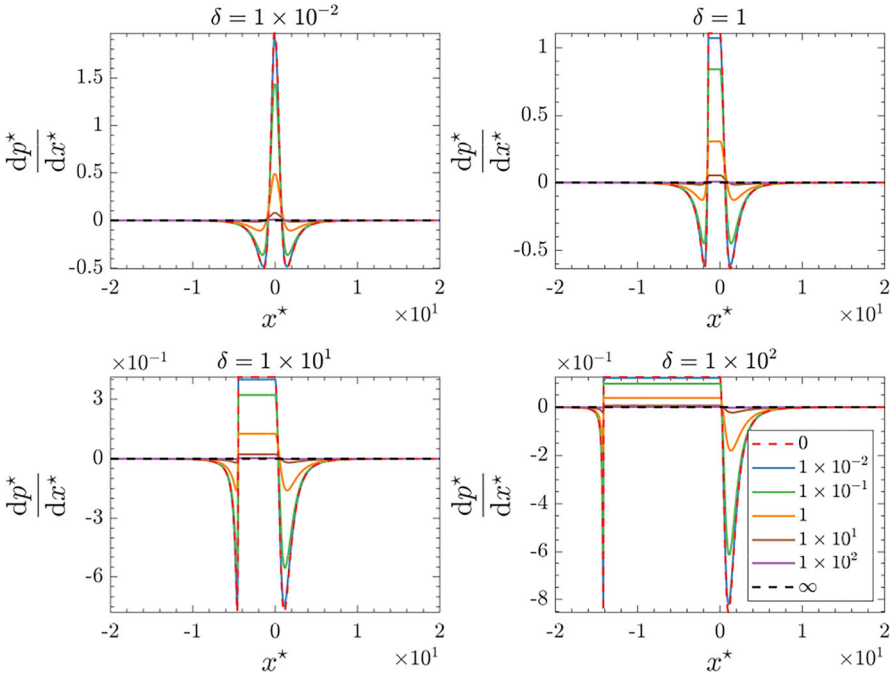

Fig. 4 Plot of the pressure derivative, $\frac{\mathrm{d}p^\star}{\mathrm{d}x^\star}$, in the inner region for different values of δ, shown in the title. The legend corresponds to the value of $\beta^\star$

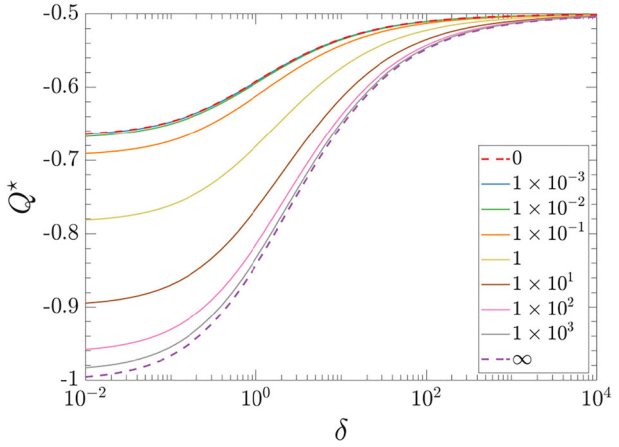

Fig. 5 Plot of the flow rate, $Q^\star$, as a function of δ. The legend corresponds to the value of $\beta^\star$

is given by

$$\lim_{\substack{\delta \to 0 \\ \beta^\star \to \infty}} Q^\star = -1, \tag{59}$$

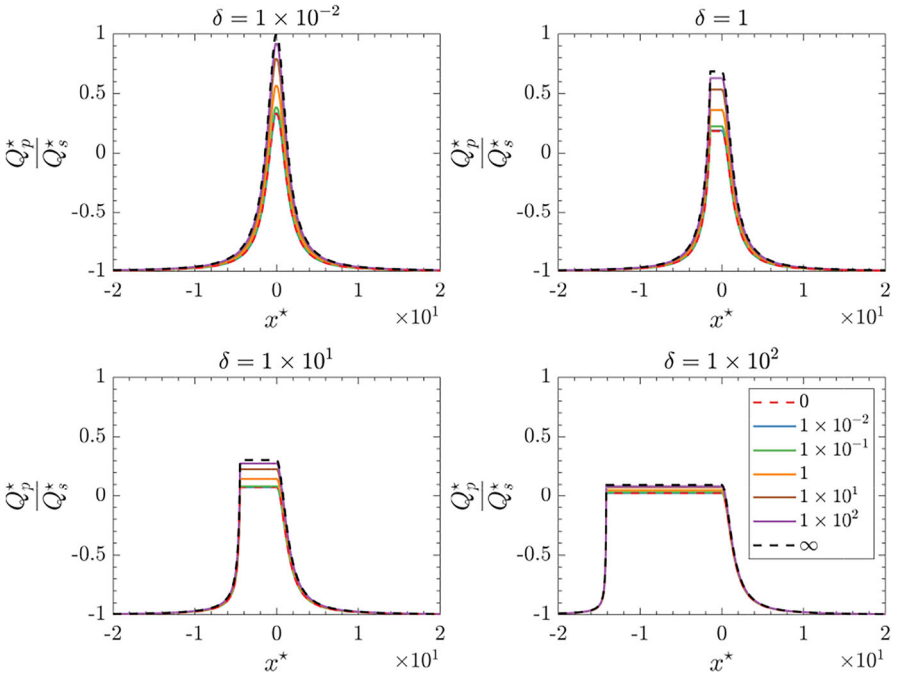

Fig. 6 Plot of the flow rate fraction, $\frac{Q_p^\star}{Q_s^\star}$, along the inner region for different values of δ, shown in the title. The legend corresponds to the value of $\beta^\star$

which occurs when there is full slip at both surfaces with depth of cut much smaller than the separation between the grinding wheel and the workpiece.

In Fig. 6, we plot the fractions of the flow rate due to pressure gradient, $Q_p^\star$, and shear effects, $Q_s^\star$.

Focussing on the grinding zone, we see from the graphs that increasing $\beta^\star$ leads to an increase in $Q_{p,2}^\star$ relative to $Q_{s,2}^\star$. This is surprising given the results shown in Fig. 4. However, it can be understood from the expression of the grinding zone flow rate given by (A.4). While the coefficient of the pressure derivative scales to infinity as $1+6\beta^\star$, using (B.14), we see the pressure derivative scales to zero as $(1+6\beta^\star)^{-1}$. These factors cancel and from these quantities with (A.8) and (A.9), we can calculate the resulting expression

$$\frac{Q_{p,2}^\star}{Q_{s,2}^\star} = -\left(1+2Q^\star\right). \tag{60}$$

Using the results for $Q^\star$ from Fig. 5, we see that an increase in $\beta^\star$ results in an increase of $Q_{p,2}^\star$ relative to $Q_{s,2}^\star$.

Expression (60) highlights the constant flow rate component fraction in the grinding zone. From this, we can calculate the fraction of the flow rate that is attributable to shear

Table 1 Values of $\frac{Q^\star_{s,2}}{Q^\star}$ for various δ and $\beta^\star$

δ	$\beta^\star$				
	0	1×10^{-1}	1	1×10^{1}	∞
0	7.5×10^{-1}	7.21×10^{-1}	6.37×10^{-1}	5.57×10^{-1}	5×10^{-1}
1×10^{-1}	7.73×10^{-1}	7.43×10^{-1}	6.57×10^{-1}	5.75×10^{-1}	5.17×10^{-1}
1	$8.44 \times 10{-}1$	8.17×10^{-1}	7.34×10^{-1}	6.52×10^{-1}	5.93×10^{-1}
1×10^{1}	9.36×10^{-1}	9.21×10^{-1}	8.72×10^{-1}	8.14×10^{-1}	7.66×10^{-1}
∞	1	1	1	1	1

Table 2 Values of $\frac{Q^\star_{p,2}}{Q^\star}$ for various δ and $\beta^\star$

δ	$\beta^\star$				
	0	1×10^{-1}	1	1×10^{1}	∞
0	2.5×10^{-1}	2.79×10^{-1}	3.63×10^{-1}	4.43×10^{-1}	5×10^{-1}
1×10^{-1}	2.27×10^{-1}	2.57×10^{-1}	3.43×10^{-1}	4.25×10^{-1}	4.83×10^{-1}
1	1.56×10^{-1}	1.83×10^{-1}	2.66×10^{-1}	3.48×10^{-1}	4.07×10^{-1}
1×10^{1}	6.4×10^{-2}	7.9×10^{-2}	1.28×10^{-1}	1.86×10^{-1}	2.34×10^{-1}
∞	0	0	0	0	0

effects and pressure gradient, denoted by $\frac{Q^\star_{s,2}}{Q^\star}$ and $\frac{Q^\star_{p,2}}{Q^\star}$, respectively. In Tables 1 and 2, the values of $\frac{Q^\star_{s,2}}{Q^\star}$ and $\frac{Q^\star_{p,2}}{Q^\star}$, respectively, are given for various parameter regimes.

As we see from the tables, it is only in the small-δ, high-$\beta^\star$ regime that there is an equal contribution to the flow rate from both pressure gradient and shear effects. Outside of this regime, the flow is predominantly driven by the motion of the grinding wheel. To illustrate this, consider a typical surface grinding regime with

$$\delta = 2, \qquad \beta^\star = 1 \times 10^{-3}, \tag{61}$$

and creep-feed grinding regime with

$$\delta = 4.8, \qquad \beta^\star = 2 \times 10^{-5}, \tag{62}$$

where we have used the values presented in Sect. 2. We find that

$$\frac{Q^\star_{p,2}}{Q^\star_{s,2}} \approx 1.44 \times 10^{-1} \tag{63}$$

for the surface grinding regime characterised by (61), and

$$\frac{Q^{\star}_{p,2}}{Q^{\star}_{s,2}} \approx 1.04 \times 10^{-1} \tag{64}$$

for the creep-feed grinding regime characterised by (62). In the surface grinding regime (61), the pressure gradient and shear effects contribute to 13% and 87% of the flow rate, respectively. In the creep-feed grinding regime (62), the pressure gradient and shear effects contribute to 9% and 91% of the flow rate, respectively.

4 Conclusion

We have studied the flow of lubricating fluid during grinding in a geometry where the depth of cut is non-zero. We have seen that we can derive a solution for the flow in the grinding zone without needing to solve for the flow outside this region. We calculated the leading order analytical solution for the pressure around the grinding zone. This was done without needing to prescribe artificial or empirically determined boundary conditions, which is the current approach employed in the literature when applying the lubrication approximation to the flow in the grinding zone.

We found that for a given δ and $\beta^{\star}$, the pressure derivative along the grinding zone is constant. As a consequence, the components of the flow rate through the grinding zone due to shear and pressure gradient are constant. We considered typical values of δ in surface and creep-feed grinding regimes, specified by (3) and (4), and calculated the contribution of each component to the flow rate through the grinding zone. We found that in both grinding regimes, the transport of the grinding fluid is primarily driven by the motion of the grinding wheel. This is shown in (63) and (64) for surface and creep-feed grinding values, respectively.

We saw that the predicted flow rate through the grinding zone increases with $\beta^{\star}$. This suggests that grinding fluids that exhibit larger degrees of slip in the grinding zone are favourable from the perspective of maximising the advection of the grinding fluid through the grinding zone. There are many studies of the mixing of additives such as nanoparticles in the grinding fluid to reduce the friction experienced by the abrasives and workpiece. For example, see [23], which shows that this results in reduced wear of the abrasives. However, there is no study of which we are aware of that investigates how such additives affect the slip length of the grinding fluid at the surfaces, and the result this has on the flow rate through the grinding zone.

Appendix A: Inner solution derivation

We integrate Eq. (40) with respect to $y^{\star}$ in each $\Omega^{\star}_i$. After using Leibniz's rule and substituting in boundary conditions (43)–(50), the additional boundary terms cancel out to leave

$$\frac{\mathrm{d}}{\mathrm{d}x^{\star}} \int_{h_1^{\star}(x^{\star})}^{h_2^{\star}(x^{\star})} u_i^{\star} \mathrm{d}y^{\star} = 0, \tag{A.1}$$

for $i = 1, 2, 3$. Equation (A.1) equivalently states that $Q_i^\star$ is constant across $\Omega_i^\star$. Using the continuity conditions (51) and (52), we see that the flow rate is constant across the inner region, i.e.

$$Q^\star = Q_1^\star = Q_2^\star = Q_3^\star, \tag{A.2}$$

where $Q^\star$ denotes the value of the constant flow rate.

From Eqs. (41) and (42), we can derive the expression for $Q_i^\star$, $i = 1, 2, 3$, as

$$Q_1^\star = \int_{h_1^\star(x^\star)}^{h_2^\star(x^\star)} u_1^\star \mathrm{d}y^\star = -\frac{x^{\star 2}+2}{4} - \frac{\left[x^{\star 2}+2\left(1+6\beta^\star\right)\right]\left(x^{\star 2}+2\right)^2}{96}\frac{\mathrm{d}p_1^\star}{\mathrm{d}x^\star}, \tag{A.3}$$

$$Q_2^\star = \int_{h_1^\star(x^\star)}^{h_2^\star(x^\star)} u_2^\star \mathrm{d}y^\star = -\frac{1}{2} - \frac{1+6\beta^\star}{12}\frac{\mathrm{d}p_2^\star}{\mathrm{d}x^\star}, \tag{A.4}$$

$$Q_3^\star = \int_{h_1^\star(x^\star)}^{h_2^\star(x^\star)} u_3^\star \mathrm{d}y^\star = -\frac{x^{\star 2}+2\left(1-\delta\right)}{4} - \frac{\left[x^{\star 2}+2\left(1+6\beta^\star-\delta\right)\right]\left[x^{\star 2}+2\left(1-\delta\right)\right]^2}{96}\frac{\mathrm{d}p_3^\star}{\mathrm{d}x^\star}, \tag{A.5}$$

respectively. We can separate each $Q_i^\star$ into two terms which describe the flow rate contribution due to shear effects, denoted $Q_{s,i}^\star$ and due to pressure gradient, denoted $Q_{p,i}^\star$. These can be expressed as

$$Q_{s,1}^\star = -\frac{x^{\star 2}+2}{4}, \tag{A.6}$$

$$Q_{p,1}^\star = -\frac{\left[x^{\star 2}+2\left(1+6\beta^\star\right)\right]\left(x^{\star 2}+2\right)^2}{96}\frac{\mathrm{d}p_1^\star}{\mathrm{d}x^\star}, \tag{A.7}$$

$$Q_{s,2}^\star = -\frac{1}{2}, \tag{A.8}$$

$$Q_{p,2}^\star = -\frac{1+6\beta^\star}{12}\frac{\mathrm{d}p_2^\star}{\mathrm{d}x^\star}, \tag{A.9}$$

$$Q_{s,3}^\star = -\frac{x^{\star 2}+2\left(1-\delta\right)}{4}, \tag{A.10}$$

$$Q_{p,3}^\star = -\frac{\left[x^{\star 2}+2\left(1+6\beta^\star-\delta\right)\right]\left[x^{\star 2}+2\left(1-\delta\right)\right]^2}{96}\frac{\mathrm{d}p_3^\star}{\mathrm{d}x^\star}. \tag{A.11}$$

Appendix B: Inner solution expressions

The solution for $p_1^\star$ is given by

$$p_1^\star = -\left\{2\left(Q^\star-3\beta^\star\right)\left(x^{\star 2}+2\right)\tan^{-1}\left(\frac{x^\star}{\sqrt{2\left(1+6\beta^\star\right)}}\right)\right.$$

$$+\sqrt{2\left(1+\beta^{\star}\right)}\left(\sqrt{2}\left(3\beta^{\star}\left(1+Q^{\star}\right)-Q^{\star}\right)\left(x^{\star 2}+2\right)\tan^{-1}\left(\frac{x^{\star}}{\sqrt{2}}\right)\right.$$
$$\left.+6\beta^{\star}Q^{\star}x^{\star}\right)\Bigg\}\Bigg/3\beta^{\star 2}\sqrt{2\left(1+6\beta^{\star}\right)}\left(x^{\star 2}+2\right)$$
$$+C_1^{\star}, \tag{B.12}$$

where

$$C_1^{\star}=\frac{\pi\left[2\left(Q^{\star}-3\beta^{\star}\right)+\sqrt{2}\sqrt{2\left(1+6\beta^{\star}\right)}\left(3\beta^{\star}\left(1+Q^{\star}\right)-Q^{\star}\right)\right]}{6\beta^{\star 2}\sqrt{2\left(1+6\beta^{\star}\right)}}. \tag{B.13}$$

The solution for $p_2^{\star}$ is given by

$$p_2^{\star}=-\frac{6\left(1+2Q^{\star}\right)x^{\star}}{1+6\beta^{\star}}+C_2^{\star}, \tag{B.14}$$

where $C_2^{\star}=C_1^{\star}$. The solution for $p_3^{\star}$ depends on the values of the parameters δ and $\beta^{\star}$, the different cases are presented below. The algebraic manipulations to derive the expression of $Q^{\star}$ in all cases were done using the software Maple [24]. As the expressions are far too arduous to present, they will not be shown here but the Maple worksheet containing the code to calculate their expressions can be found at [25].

Solution for $0<\delta<1$

In this case,

$$p_3^{\star}=-2\Bigg\{\left(Q^{\star}-3\beta^{\star}\right)\left(1-\delta\right)\sqrt{2\left(1-\delta\right)}\left[x^{\star 2}+2\left(1-\delta\right)\right]$$
$$\times\tan^{-1}\left(\frac{x^{\star}}{\sqrt{2\left(1+6\beta^{\star}-\delta\right)}}\right)+\sqrt{2\left(1+6\beta^{\star}-\delta\right)}\Bigg[$$
$$\left(\delta\left(Q^{\star}-3\beta^{\star}\right)+3\beta^{\star}\left(1+Q^{\star}\right)-Q^{\star}\right)\left[x^{\star 2}+2\left(1-\delta\right)\right]\tan^{-1}\left(\frac{x^{\star}}{\sqrt{2\left(1-\delta\right)}}\right)$$
$$+3\beta^{\star}Q^{\star}\sqrt{2\left(1-\delta\right)}x^{\star}\Bigg]\Bigg\}$$
$$\Bigg/3\beta^{\star 2}\left(1-\delta\right)\sqrt{2\left(1-\delta\right)}\sqrt{2\left(1+6\beta^{\star}-\delta\right)}\left[x^{\star 2}+2\left(1-\delta\right)\right]$$
$$+C_3^{\star}, \tag{B.15}$$

where

$$C_3^{\star}=-\pi\Bigg\{\sqrt{2\left(1+6\beta^{\star}-\delta\right)}\left(\delta\left(Q^{\star}-3\beta^{\star}\right)+3\beta^{\star}\left(1+Q^{\star}\right)-Q^{\star}\right) \tag{B.16}$$

$$+\left(Q^\star-3\beta^\star\right)(1-\delta)\sqrt{2\,(1-\delta)}\Big\} \tag{B.17}$$

$$\Big/\,3\beta^{\star 2}\,(1-\delta)\sqrt{2\,(1-\delta)}\sqrt{2\,(1+6\beta^\star-\delta)}. \tag{B.18}$$

Solution for $\delta = 1$

In this case,

$$p_3^\star = -\frac{\sqrt{3}\,(Q^\star-3\beta)\,x^{\star 3}\tan^{-1}\left(\frac{x^\star}{2\sqrt{3\beta^\star}}\right)+6\sqrt{\beta^\star}\left[Q^\star x^{\star 2}-\beta\left(3x^{\star 2}+4Q^\star\right)\right]}{9\beta^{\star\frac{5}{2}}x^{\star 3}} + C_3^\star, \tag{B.19}$$

where

$$C_3^\star = -\frac{\pi\sqrt{3}\,(Q^\star-3\beta^\star)}{18\beta^{\star\frac{5}{2}}}. \tag{B.20}$$

Solution for $1 < \delta < 1+6\beta^\star$

For $1 < \delta < 1+6\beta^\star$, we note that

$$\left|\frac{x^\star}{\sqrt{2\,(\delta-1)}}\right| > 1$$

for $x^\star < x_L^\star$. In this case,

$$\begin{aligned} p_3^\star = &-2\Big\{\left(Q^\star-3\beta^\star\right)(\delta-1)\sqrt{2\,(\delta-1)}\left[x^{\star 2}-2\,(\delta-1)\right] \\ &\times\tan^{-1}\left(\frac{x^\star}{\sqrt{2\,(1+6\beta^\star-\delta)}}\right)+\sqrt{2\,(1+6\beta^\star-\delta)}\Big[\\ &\left(\delta\left(Q^\star-3\beta^\star\right)+3\beta^\star\left(1+Q^\star\right)-Q^\star\right)\left[x^{\star 2}-2\,(\delta-1)\right] \\ &\times\coth^{-1}\left(\frac{x^\star}{\sqrt{2\,(\delta-1)}}\right)-3\beta^\star Q^\star\sqrt{2\,(\delta-1)}x^\star\Big]\Big\} \\ &\Big/\,3\beta^{\star 2}\,(\delta-1)\sqrt{2\,(\delta-1)}\sqrt{2\,(1+6\beta^\star-\delta)}\left[x^{\star 2}-2\,(\delta-1)\right] \\ &+C_3^\star, \end{aligned} \tag{B.21}$$

where

$$C_3^\star = -\frac{\pi\left(Q^\star - 3\beta^\star\right)}{3\beta^{\star 2}\sqrt{2\left(1+6\beta^\star-\delta\right)}}. \tag{B.22}$$

Solution for $\delta = 1 + 6\beta^\star$

For $\delta = 1 + 6\beta^\star$, we note that

$$\left|\frac{x^\star}{2\sqrt{3\beta^\star}}\right| > 1$$

for $x^\star < x_L^\star$. In this case,

$$\begin{aligned} p_3^\star = &\left\{2Q^\star\sqrt{\beta^\star}x^{\star 2} + \left(x^{\star 2} - 12\beta^\star\right)\left[\sqrt{3}\left(2\beta^\star - Q^\star\right)x^\star\right.\right. \\ &\left.\left.\times \coth^{-1}\left(\frac{x^\star}{2\sqrt{3\beta^\star}}\right) - 4\left(3\beta^\star - Q^\star\right)\sqrt{\beta^\star}\right]\right\} \\ &\Big/ 6\beta^{\star\frac{5}{2}}x^\star\left(x^{\star 2} - 12\beta^\star\right) \\ &+ C_3^\star, \end{aligned} \tag{B.23}$$

where

$$C_3^\star = 0. \tag{B.24}$$

Solution for $\delta > 1 + 6\beta^\star$

For $\delta > 1 + 6\beta^\star$, we note that

$$\left|\frac{x^\star}{\sqrt{2\left(\delta-1\right)}}\right| > 1,$$
$$\left|\frac{x^\star}{\sqrt{2\left[\delta-\left(1+6\beta^\star\right)\right]}}\right| > 1$$

for $x^\star < x_L^\star$. In this case,

$$\begin{aligned} p_3^\star = 2\Bigg\{ &\left(Q^\star - 3\beta^\star\right)\left(\delta-1\right)\sqrt{2\left(\delta-1\right)}\left[x^{\star 2} - 2\left(\delta-1\right)\right] \\ &\times \coth^{-1}\left(\frac{x^\star}{\sqrt{2\left[\delta-\left(1+6\beta^\star\right)\right]}}\right) - \sqrt{2\left[\delta-\left(1+6\beta^\star\right)\right]}\Big[\\ &\left(\delta\left(Q^\star - 3\beta^\star\right) + 3\beta^\star\left(1+Q^\star\right) - Q^\star\right)\left[x^{\star 2} - 2\left(\delta-1\right)\right] \end{aligned}$$

$$\times \coth^{-1}\left(\frac{x^\star}{\sqrt{2\,(\delta-1)}}\right) - 3\beta^\star Q^\star \sqrt{2\,(\delta-1)}x^\star\Bigg]\Bigg\}$$
$$\Big/ 3\beta^{\star 2}\,(\delta-1)\sqrt{2\,(\delta-1)}\sqrt{2\,[\delta-(1+6\beta^\star)]}\left[x^{\star 2}-2\,(\delta-1)\right]$$
$$+ C_3^\star, \tag{B.25}$$

where

$$C_3^\star = 0. \tag{B.26}$$

Appendix C: Numerical validation

To validate the lubrication model that we derived in Sect. 2, we will compare the inner region pressure solution given by (B.12), (B.14), (B.15), (B.19), (B.21), (B.23) and (B.25) to the pressure solution of the full-scale problem given by (16)–(21) for different parameter regimes. We will only consider the steady full-scale problem as the time dependency is expected to be negligible in the grinding zone. We remark that, due to the lubrication approximation, the pressure values of the full-scale problem that we present will be the cross-sectional average of the pressure solution between the workpiece and the grinding wheel.

In order to numerically solve the full-scale problem, we replace the far-field boundary conditions by representative boundary conditions on an artificial boundary which truncates the flow domain Ω. To this end, we impose the no-stress boundary condition

$$\boldsymbol{n}\cdot\left(-p\boldsymbol{I}+2\varepsilon^{\frac{3}{2}}\boldsymbol{E}\right)=\boldsymbol{0} \qquad \text{on } \Gamma_A, \tag{C.27}$$

where

$$\begin{aligned}\Gamma_A = &\left\{(x,y): x=-2.5,\ y\in\left[\gamma,3\right]\right\}\\ &\cup\left\{(x,y): x\in[-2.5,3.5],\ y=3\right\}\\ &\cup\left\{(x,y): x=3.5,\ y\in[0,3]\right\},\end{aligned} \tag{C.28}$$

with γ defined by (2). The artificial boundary Γ_A is chosen sufficiently far from the grinding zone to minimise its influence on the flow in the grinding zone. The (modified) full-scale problem given by (16)–(19), (C.27) is then solved using the continuous Galerkin finite element method [26].

The three parameter regimes we consider are

$$\text{Regime 1:}\quad \varepsilon = 5\times10^{-5}, \qquad \delta = 2, \qquad \mathrm{Re} = 1\times10^{3}, \tag{C.29}$$
$$\text{Regime 2:}\quad \varepsilon = 2.5\times10^{-3}, \qquad \delta = 4.8, \qquad \mathrm{Re} = 4\times10^{2}, \tag{C.30}$$
$$\text{Regime 3:}\quad \varepsilon = 1\times10^{-3}, \qquad \delta = 10, \qquad \mathrm{Re} = 1\times10^{3}. \tag{C.31}$$

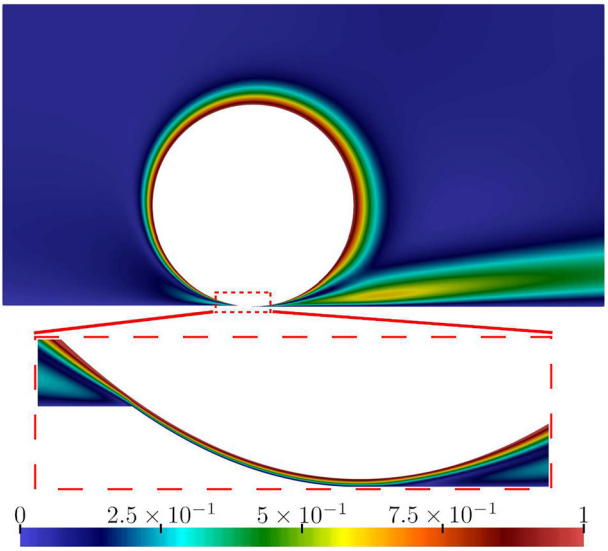

Fig. 7 Plot of the velocity magnitude from the full-scale solution of the Navier–Stokes equations. Inside the dashed region, the grinding zone has been magnified and stretched along the y-axis for visualisation

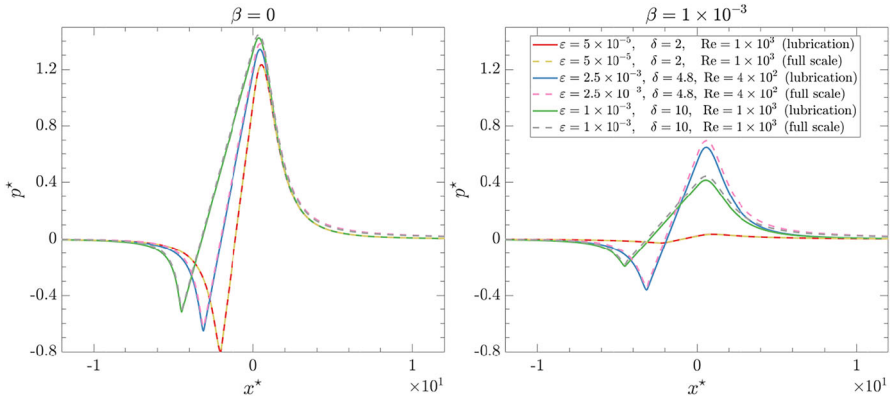

Fig. 8 Plot of the pressure solution, $p^\star$, from the lubrication model (solid lines) and the full-scale problem (dashed lines) for different parameter regimes shown in the legend and plot titles

For parameter regimes 2 and 3, we have taken $\mathrm{Re} = \varepsilon^{-1}$ following (6). For parameter regime 1, the flow becomes unsteady for larger Re hence we take $\mathrm{Re} = 1 \times 10^3$ to be able to calculate a steady full-scale solution. In Fig. 7, we show an example of the full-scale problem's flow field via a plot of the velocity magnitude for parameter regime 3 with $\beta = 0$.

In Fig. 8, we plot the pressure solution of the lubrication model and full-scale problem for parameter regimes 1–3 and two slip lengths, $\beta = 0, 1 \times 10^{-3}$, where (32) has been used for rescaling variables. We emphasise that the relevant slip length around the grinding zone, i.e. the stretched slip length $\beta^\star$, depends on both β and ε.

Table 3 Maximum difference between the pressure solution, $p^\star$, of the lubrication model and full-scale problem for $x^\star \in \left[-1.2 \times 10^1, 1.2 \times 10^1\right]$

Regime	β	
	0	1×10^{-3}
1	4.86×10^{-4}	1.22×10^{-3}
2	4.38×10^{-2}	5.29×10^{-2}
3	3.15×10^{-2}	3.15×10^{-2}

Qualitatively, we see that the pressure solutions of the lubrication model and the full-scale problem match well across the parameter regimes. Notably, linearity of the pressure solution in the grinding zone is seen in the full-scale problem, as we noted for the lubrication model in Sect. 3.

In Table 3, we present the maximum difference between the pressure solutions shown in Fig. 8 for each parameter regime. As expected, the greatest difference between the solutions occurs in the regime with the largest ε, i.e. regime 2. However, the difference between solutions in all regimes is small.

Acknowledgements The authors express their gratitude to Professor Dragos Axinte, University of Nottingham, for constructive discussions on machining processes.

Author Contributions J.B. and P.H. conceived and designed the study; J.B. and Z.C. interpreted results; Z.C prepared draft manuscript, performed the analysis, gathered and analysed results and prepared figures; All authors edited and reviewed the manuscript.

Data availability No datasets were generated or analysed during the current study.

Declarations

Conflict of interest The authors declare no competing interests.

References

1. Malkin S, Guo C (2007) Thermal analysis of grinding. CIRP Ann-Manuf Technol 56(2):760–782
2. Klocke F, Eisenblätter G (1997) Dry cutting. CIRP Ann-Manuf Technol 46(2):519–526
3. Chang CC, Wang SH, Szeri AZ (1996) On the mechanism of fluid transport across the grinding zone. J Manuf Sci Eng 118(3):332–338
4. Engineer F, Guo C, Malkin S (1992) Experimental measurement of fluid flow through the grinding zone. J Eng Ind 114:61–66

5. Reynolds O (1886) On the theory of lubrication and its application to Mr. Beauchamp tower's experiments, including an experimental determination of the viscosity of olive oil. Philos Trans R Soc 177:157–235
6. Leal LG (2007) Advanced transport phenomena: fluid mechanics and convective transport processes. Cambridge University Press, Cambridge
7. Tavakol B, Froehlicher G, Holmes DP, Stone HA (2017) Extended lubrication theory: improved estimates of flow in channels with variable geometry. Proc R Soc A 473(2206):20170234
8. Tuck EO, Bentwich M (1983) Sliding sheets: lubrication with comparable viscous and inertia forces. J Fluid Mech 135:51–69
9. Schumack MR, Chung J, Schultz WW, Kannatey-Asibu E Jr (1991) Analysis of fluid flow under a grinding wheel. J Eng Ind 113(2):190–197
10. Hryniewicz P, Szeri AZ, Jahanmir S (2000) Application of lubrication theory to fluid flow in grinding: part i—flow between smooth surfaces. J Tribol 123(1):94–100
11. Hryniewicz P, Szeri AZ, Jahanmir S (2000) Application of lubrication theory to fluid flow in grinding: part ii—influence of wheel and workpiece roughness. J Tribol 123(1):101–107
12. Guo C, Malkin S (1992) Analysis of fluid flow through the grinding zone. J Ind Eng Int 114(4):427–434
13. Vesali A, Tawakoli T (2014) Study on hydrodynamic pressure in grinding contact zone considering grinding parameters and grinding wheel specifications. Procedia CIRP 14:13–18
14. Gviniashvili VK, Woolley NH, Rowe WB (2004) Useful coolant flowrate in grinding. Int J Mach Tools Manuf 44(6):629–636
15. Howes TD, Neailey K, Harrison AJ, McKeown PA (1987) Fluid film boiling in shallow cut grinding. CIRP Ann 36(1):223–226
16. Marinescu ID, Rowe WB, Dimitrov B, Ohmori H (2013) Tribology of abrasive machining processes, 2nd edn. Elsevier, Amsterdam
17. Lauga E, Brenner M, Stone H (2007) Microfluidics: the no-slip boundary condition. In: Tropea C, Yarin AL, Foss JF (eds) Springer handbook of experimental fluid mechanics. Springer, Berlin, pp 1219–1240
18. Wichmann M, Eden M, Zvegincev D, Wiesener F, Bergmann B, Schmidt A (2023) Modeling the wetting behavior of grinding wheels. Int J Adv Manuf Technol 128:1741–1747
19. Nadolny K, Kapłonek W, Królczyk G, Ungureanu N (2018) The effect of active surface morphology of grinding wheel with zone-diversified structure on the form of chips in traverse internal cylindrical grinding of 100cr6 steel. Proc Inst Mech Eng B 232(6):965–978
20. Saravanakumar A, Dhanabal S, Jayanand E, Logeshwaran P (2018) Analysis of process parameters in surface grinding process. Mater Today Proc 5(2):8131–8137
21. Grigoriev SN, Starkov VK, Gorin NA, Krajnik P, Kopač J (2013) Creep-feed grinding: an overview of kinematics, parameters and effects on process efficiency. Stroj Vestn—J Mech Eng 60(4):213–220
22. Abou-Dina MS, Helal MA, Ghaleb AF, Kaoullas G, Georgiou GC (2020) Newtonian plane couette flow with dynamic wall slip. Meccanica 55(7):1499–1507
23. Dongkun Z, Changhe L, Dongzhou J, Yanbin Z, Xiaowei Z (2014) Specific grinding energy and surface roughness of nanoparticle jet minimum quantity lubrication in grinding. Chin J Aeronaut 28(2):570–581
24. Maplesoft, a division of Waterloo Maple Inc.: Maple 2021.0. Waterloo, Ontario
25. Crowson Z (2024) Grinding flow rate calculations. GitHub
26. Brenner SC, Scott LR (2008) The mathematical theory of finite element methods, 3rd edn. Springer, New York